Supporting Information

van der Heijden 10.1073/pnas.1412412111

SI Text

Model Description and Parameters. *Stiffness and damping.* The elastic beams have no longitudinal coupling or flexural stiffness. Their elastic behavior is described by their individual stiffness per unit length along the propagation direction, s_1 and s_2. The same holds for the coupling between the beams s_{12}. The values used were s_1 = 5.2 kN/m^2, s_2 = 15.1 kN/m^2, s_{12} = 75.4 kN/m^2 for the calculations underlying Figs. 3 and 4. This corresponds to a ratio s_1:s_2:s_{12} of 1:3:14, and to a net stiffness per unit length (probed by pushing beam 1 only) of 20 kN/m^2. The latter value matches stiffness measurements of the basilar membrane in the basal turn of the gerbil (1). Spatial variation of stiffness was described by $s(x) = s(0)\exp(-2\alpha x)$, with α = 0.46 mm^{-1}, based on the frequency-place map of the gerbil (2). The damping associated with beam velocity is captured by the two damping coefficients λ and μ described following Eq. **S21**. Their values are $\lambda = 3\mu = 9.7$ Ns/m^2.
Geometry and specific fluid mass. (For model layout, see Fig. 1.) Diameter of the half-cylindrical chambers: 500 μm; width of the slit connecting the chambers: $w = 60$ μm; height of the slit: $h = 50$ μm. This geometry was motivated by the basal turn of the gerbil cochlea (3). Beam displacement profile was proportional to $\varsigma(y)=\exp(-(y/b)^2/2)$, with y the coordinate along the width of the beams ($y = 0$ corresponding to the center) and $b = 35$ μm. This was motivated by radial profiles of basilar membrane motion in the basal turn of the gerbil (4). Specific mass of the fluid: ρ = 1,000 kg/m^3.

Analysis of Fluid Motion. *Fanning waves and their dispersion.* With only a single chamber filled with fluid, the waveguide supports a type of 3D fluid wave analyzed by Steele and Taber (5). For sufficiently small wavelength, the waves are deep (i.e., the rigid boundaries become irrelevant), and the fluid particles describe circles that lie in planes perpendicular to the plane of view in Fig. 1. The projection of the circular trajectories onto the waveguide cross-section produces a fanning pattern as shown in Fig. S1. The dispersion of these fanning waves is determined by the dependence of the effective fluid mass on wavenumber (m_{ch} curve in Fig. 2). An illustrative metric of the degree of dispersion is the ratio U/c of group velocity U and phase velocity c. For non-dispersive waves U/c = 1; for deep plane waves U/c = 0.5, independent of wavenumber. For the fanning waves, U/c varies with wavenumber k as shown in Fig. S2. The minimum value of U/c depends on the width of the beam displacement profile. The model geometry used here has a minimum U/c value of 0.16.
Effective fluid mass. Fluid motion was determined by solving the Laplace equation for the velocity potential Φ describing irrotational fluid motion (6):

$$\nabla^2\Phi = 0. \qquad \text{[S1]}$$

Fluid velocity $\mathbf{u}$ is the gradient of Φ

$$\mathbf{u} = \nabla\Phi. \qquad \text{[S2]}$$

The boundary conditions are

$$\mathbf{n}\cdot\nabla\Phi = 0 \quad \text{(rigid boundaries)}, \qquad \text{[S3a]}$$

$$\partial\Phi/\partial z = \varsigma(y)\dot{\eta}_m \quad \text{(beams)}, \qquad \text{[S3b]}$$

where $\varsigma(y)$ is the normalized displacement profile of the beams (*Model Description and Parameters*), $\mathbf{n}$ is the outward normal, and η_1 and η_2 are the transverse displacements of the center of beam 1 and 2, respectively. The dot denotes the time derivative. For harmonic traveling waves traveling in the x direction, having angular frequency ω and wavenumber of k,

$$\Phi(x,y,z,t) = \mathrm{Re}\left(e^{i\omega t - ikx}\phi(y,z)\right), \qquad \text{[S4]}$$

and the 3D Laplace equation for Φ (Eq. **S1**) reduces to a 2D Helmholtz equation for ϕ

$$\left(\frac{\partial^2}{\partial y^2}+\frac{\partial^2}{\partial z^2}\right)\phi(y,z) = k^2\phi(y,z). \qquad \text{[S5]}$$

The geometry of Fig. 1 applies to this problem; denoting the vertical (z) positions of the two beams by $\pm h/2$ and their width by w, the boundary conditions of this 2D problem are

$$\begin{aligned}&\frac{\partial\phi}{\partial n} = 0 \text{ at rigid boundaries;}\\ &\frac{\partial\phi}{\partial z} = \varsigma(y)\dot{\eta}_1,\ z = +h/2;\ -w/2<y<w/2\\ &\qquad\varsigma(y)\dot{\eta}_2,\ z = -h/2;\ -w/2<y<w/2\\ &\qquad 0, \text{ elsewhere.}\end{aligned} \qquad \text{[S6]}$$

Eqs. **S5** and **S6** describe the motion of the fluid in both chambers and the slit. This problem was solved numerically using triangulation (PDE toolbox in MATLAB). Owing to the geometric symmetry and the linearity of the problem, it was sufficient to restrict these calculations to $\dot{\eta}_1 = 1$; $\dot{\eta}_2 = 0$, i.e., only the upper beam moving at unit velocity. The real-valued solution to this reduced problem for ϕ in the upper half-cylindrical chamber will be denoted by $\phi_{ch}(y,z;k)$. This is the solution portrayed in Fig. S2. The kinetic energy in the chamber per unit length in the x direction, averaged over one cycle, is

$$\langle T_{ch}(k)\rangle = \frac{\dot{\eta}_1^2}{4}\rho\int_{CH} dydz\left[k^2 + (\partial\phi_{ch}/\partial y)^2 + (\partial\phi_{ch}/\partial z)^2\right], \qquad \text{[S7]}$$

where the braces denote time averaging. The integral is taken over the cross-section of the chamber. The integrand is the squared magnitude of the fluid velocity. Because $\dot{\eta}_1$ is the velocity of the beam, Eq. **S7** has the familiar form $T = 1/2(mv^2)$ (the additional factor 1/2 comes from time averaging). The effective fluid mass of the fluid in the chamber is therefore

$$m_{ch}(k) = \rho\int_{CH} dydz\left[k^2 + (\partial\phi_{ch}/\partial y)^2 + (\partial\phi_{ch}/\partial z)^2\right]. \qquad \text{[S8]}$$

Eq. **S8** was used to compute $m_{ch}(k)$ shown in Fig. 2.
Fluid between the beams. Fluid motion in the slit (Fig. 1*B*) is affected by the motion of both beams. Starting again with $\dot{\eta}_1 = 1$; $\dot{\eta}_2 = 0$ (only upper beam moving), denote the real-valued solution of the 2D problem (Eqs. **S5** and **S6**) by $\phi_1(y,z;k)$. This particular solution ϕ_1 of the Helmholtz equation was obtained numerically for a large range of k values. The solution $\phi_2(y,z;k)$ for the case where the other beam is moving ($\dot{\eta}_1 = 0$; $\dot{\eta}_2 = 1$) follows from the geometric symmetry:

$$\phi_2(y,z;k) = -\phi_1(y,-z;k). \qquad \textbf{[S9]}$$

The general solution of Eqs. **S5** and **S6**, in which both beams move, becomes

$$\phi = \dot{\eta}_1\phi_1 + \dot{\eta}_2\phi_2, \qquad \textbf{[S10]}$$

where phase differences between beam motion are realized by complex η_1 and η_2.

The kinetic energy of a transversal slice S of fluid equals

$$\begin{aligned} T\mathrm{d}x &= \frac{\rho}{2}\iiint_S \mathrm{d}V(\nabla\Phi)^2 \\ &= \frac{\rho}{2}\iiint_S \mathrm{d}V\nabla(\Phi\nabla\Phi) \\ &= \frac{\rho}{2}\iint_{\delta S} \mathrm{d}\mathbf{n}\cdot\Phi\nabla\Phi, \end{aligned} \qquad \textbf{[S11]}$$

where Eq. **S1** and the divergence theorem were used, **n** is the outward unit normal, and dx is the thickness of the slice. Given the dependence of Φ on x and t (Eq. **S4**), the contributions of the YZ planes of the boundaries of the slice cancel when averaged over a period, leaving only the contributions of the boundaries of the slit. Taking the limit of vanishing dx, the expression for T becomes a line integral along the boundaries of the cross-section of the slit. Because the integrand vanishes at the rigid boundaries, the only contributions to the integral come from the beams B1 and B2. Using Eq. **S4**, one obtains

$$\langle T\rangle = \frac{\rho}{4}\int_{B1+B2} \mathrm{d}s\,\mathrm{Re}(\phi^*\,\partial\phi/\partial n), \qquad \textbf{[S12]}$$

where $\partial\phi/\partial n$ is the gradient of ϕ along the outward normal, the asterisk denotes complex conjugation, and where I used the identity

$$\left\langle \mathrm{Re}\left(ae^{i\omega t}\right)\mathrm{Re}\left(be^{i\omega t}\right)\right\rangle = 1/2\langle\mathrm{Re}(a^*b)\rangle. \qquad \textbf{[S13]}$$

Combining Eqs. **S10** and **S12**, and using $\partial\phi_2/\partial n = 0$ at B1 and $\partial\phi_1/\partial n = 0$ at B2, one obtains

$$\langle T\rangle = 1/4\left(\dot{\eta}_1^* m_1\dot{\eta}_1 + \dot{\eta}_1^* m_{12}\dot{\eta}_2 + \dot{\eta}_2^* m_{21}\dot{\eta}_1 + \dot{\eta}_2^* m_2\dot{\eta}_2\right), \qquad \textbf{[S14]}$$

with

$$\begin{aligned} m_1 &= \rho\int_{B1} \mathrm{d}s\;\phi_1\;\partial\phi_1/\partial n \\ m_2 &= \rho\int_{B2} \mathrm{d}y\;\phi_2\partial\phi_2/\partial n \\ m_{12} &= \rho\int_{B2} \mathrm{d}y\;\phi_1\partial\phi_2/\partial n \\ m_{21} &= \rho\int_{B1} \mathrm{d}y\;\phi_2\partial\phi_1/\partial n. \end{aligned} \qquad \textbf{[S15]}$$

Using the symmetry (Eq. **S9**) and the boundary conditions (Eq. **S6**), this reduces to

$$\begin{aligned} m_1 = m_2 = m_{\mathrm{tr}}(k) &= \rho\int_{-w/2}^{w/2} \mathrm{d}y\;\varsigma(y)\phi_1(y,(1/2)h;k) \\ m_{12} = m_{21} = -m_{\mathrm{cpl}}(k) &= -\rho\int_{-w/2}^{w/2} \mathrm{d}y\;\varsigma(y)\phi_1(y,-(1/2)h;k). \end{aligned} \qquad \textbf{[S16]}$$

The second line of Eq. **S16** exposes the mass-loading nature of the coupling between the beams; it represents the integrated product of two factors. The first factor is the fluid pressure (the time derivative of ϕ) evoked by the motion of one beam, evaluated at the position of the opposite beam. The second factor is the transversal velocity of the opposite beam. Eq. **S16** was used to compute $m_{\mathrm{tr}}(k)$ and $m_{\mathrm{cpl}}(k)$ shown in Fig. 2. In matrix notation, and after including the contribution the fluid of both chambers (Eq. **S8**), the time-averaged kinetic energy (Eq. **S14**) becomes

$$\langle T\rangle = (1/4)\dot{\eta}^\dagger M(k)\dot{\eta}, \qquad \textbf{[S17]}$$

where the dagger denotes Hermitian conjugation, and the mass matrix M is given in Eq. **1** of the main text. The negative sign of the off-diagonal (coupling) term of M reflects the reduction of effective fluid mass when both beams move in phase (compared with the case with only one beam moving). The parallel beam motion alleviates the squirting of the fluid.

Elastic Coupling and Damping. ***Stiffness matrix.*** Given beam displacements η_1 and η_2, individual beam stiffness values s_1 and s_2, and coupling s_{12}, the potential energy per unit length equals

$$V = 1/2\left[s_1\eta_1^2 + s_2\eta_2^2 + s_{12}(\eta_1-\eta_2)^2\right]. \qquad \textbf{[S18]}$$

Generalizing to complex displacement values to describe harmonic motion, and using Eq. **S13**, the time-averaged potential energy becomes

$$<V> = 1/4\left(\eta^\dagger S(k)\eta\right), \qquad \textbf{[S19]}$$

with the stiffness matrix S given in Eq. **3** of the main text.

Damping. The equation of motion for the beam displacement η is

$$M\ddot{\eta} + D\dot{\eta} + S\eta = 0, \qquad \textbf{[S20]}$$

where the damping matrix D, which quantifies the damping force per unit length per unit beam velocity, equals

$$\begin{aligned} D &= R\begin{pmatrix}\lambda & 0\\ 0 & \mu\end{pmatrix}R^{-1}; \\ R &= \begin{pmatrix}\cos 2\pi\beta & \sin 2\pi\beta\\ -\sin 2\pi\beta & \cos 2\pi\beta\end{pmatrix}. \end{aligned} \qquad \textbf{[S21]}$$

This form of D has two principal values λ and μ that apply to two orthogonal vibration mode shapes. In this study, β = 0.3 cycle and $\lambda = 3\mu = 9.7$ Ns/m^2. This form of D damps the A mode more than the P mode. Thus, damping is predominantly associated with an antiparallel beam motion, as if a dashpot is mounted next to the spring in Fig. 1*B*. Damping was evaluated as a perturbation of the undamped configuration, i.e., Eq. **S20** was treated as a perturbation of the $D = 0$ case. Denoting the normalized eigenmodes of the unperturbed case by $\eta^{(1)}$ and $\eta^{(2)}$, their dot

product by χ, and their respective eigenvalues by $\omega^{(1)}$ and $\omega^{(2)}$, first-order perturbation yields

$$\omega^{(n)} \to \omega^{(n)} + \Delta^{(n)},$$
$$\Delta^{(n)} = \frac{i}{2(1-\chi^2)}\left(\eta^{(n)} - \chi\eta^{(3-n)}\right)^{\dagger} M^{-1} D\eta^{(n)}. \quad \text{[S22]}$$

Because the eigenmodes of the unperturbed case are real, and so are M and D, Eq. **S22** implies that damping causes the frequency to acquire an imaginary part, describing the temporal decay of standing waves. To assess the corresponding spatial decay of traveling waves, one must find the perturbation of the wavenumber k that restores the temporal periodicity, as analyzed by Lighthill (6), chapter 3.6:

$$k^{(n)} \to k^{(n)} - \Delta^{(n)}/U^{(n)},$$
$$U = \partial\omega/\partial k. \quad \text{[S23]}$$

Physically, $\mathrm{Im}(\omega)$ describes the temporal rate of energy loss, which is related to the spatial rate of loss via the travel speed of the energy, the group velocity U.

Wave Propagation in the Model. ***Solving Eq. 4.*** Eq. **4** (main text) describes the propagation of the waves by decomposing arbitrary beam displacements into normal mode contributions and applying the spatial gradients of the two normal modes. It was solved numerically by dividing a 4-mm length of the waveguide in 500 segments and approximating the spatial derivatives by finite differences. Two independent solutions $\eta^{(1)}(x)$ and $\eta^{(2)}(x)$ were determined by using the respective initial conditions

$$\eta^{(1)}(0) = \begin{pmatrix} 1 \\ 0 \end{pmatrix}; \quad \eta^{(2)}(0) = \begin{pmatrix} 0 \\ 1 \end{pmatrix}. \quad \text{[S24]}$$

From these two particular solutions, the solution having an arbitrary initial condition $\eta^{A}(0)$ is obtained by

$$\eta^{A}(x) = \mathrm{E}(x)\eta^{A}(0), \quad \text{[S25]}$$

where the matrix E is given by

$$\mathrm{E}_{ij}(x) = \eta_i^{(j)}(x). \quad \text{[S26]}$$

E(x) contains the complete solution of Eq. **4**. It can be used, by inversion, to find those initial conditions at $x = 0$ that produce a given propagation mode at any location x_A within the waveguide, and specifically, to find the initial condition that causes the wave to be in the AP mode before entering its region of mode shape swapping. The 24-kHz wave shown in Fig. 5 was presented at $x = 0$ in the mode shape that causes it to be purely in the AP mode at $x = 1$ (Fig. S3). The other two waves (17 and 33 kHz) were presented in that same mode shape that presumably favors the peaking of 24-kHz waves. Their propagation behavior shows that aiming for the exact AP mode is not necessary for creating the peak.

Mode conversion and choice of initial condition. In Fig. S3 the model responses of Fig. 5 are decomposed into the contributions of the AP and PA modes. The spatial variation of the two components illustrates mode conversion, but is also affected by the different propagation properties of the individual modes: their group velocity, effective stiffness, and damping. The fact that the 24-kHz wave (green curve), which is exactly in the AP mode at $x = 1$, has nonvanishing PA components both at $x < 1$ and $x > 1$ shows that a certain amount of mode conversion does occur. However, it is obvious that mode conversion does not affect the peaking, because the dominance of the AP mode persists up to locations well beyond the peak. Eventually, the steeper decay of the AP mode causes the PA mode to become dominant (circles).

Alternative waveguide geometries. The waveguide geometry shown in Fig. 1 was not chosen for its physiological resemblance to the mammalian inner ear, but for its simplicity; it possesses the bare essentials needed to realize mode shape swapping. As detailed in *Discussion*, there exist many alternative geometries that are capable of showing the same physical behavior. Fig. S4 illustrates some of those alternatives. Note that, in contrast with the model in Fig. 1, many of the examples involve a combination of horizontal and vertical deformation. Moreover, most of the mode shapes shown give rise to fanning and squirting waves even if they are only surrounded by fluid on one side. Thus, the presence of two opposing fluid chambers is not a strict necessity, and the physics of mode shape swapping may play a role in nonmammalian ears as well.

1. Emadi G, Richter CP, Dallos P (2004) Stiffness of the gerbil basilar membrane: Radial and longitudinal variations. *J Neurophysiol* 91(1):474–488.
2. Müller M (1996) The cochlear place-frequency map of the adult and developing Mongolian gerbil. *Hear Res* 94(1-2):148–156.
3. Plassmann W, Peetz W, Schmidt M (1987) The cochlea in gerbilline rodents. *Brain Behav Evol* 30(1-2):82–101.
4. Ren T, He W, Gillespie PG (2011) Measurement of cochlear power gain in the sensitive gerbil ear. *Nat Commun* 2:216.
5. Steele CR, Taber LA (1979) Comparison of WKB calculations and experimental results for three-dimensional cochlear models. *J Acoust Soc Am* 65(4):1007–1018.
6. Lighthill J (1978) *Waves in Fluids* (Cambridge Univ Press, Cambridge, UK).

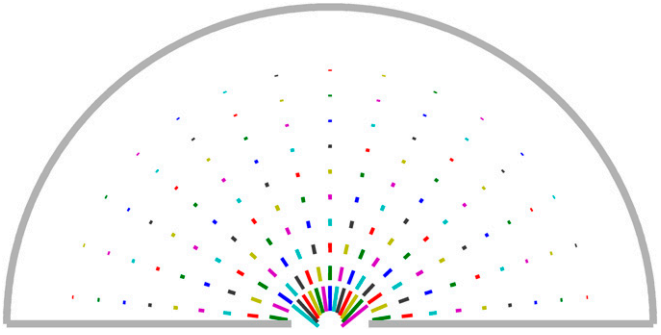

Fig. S1. Fanning wave pattern of fluid motion. Colored lines are the projections on the plane of view of the circular trajectories of fluid particles in the upper chamber of the model waveguide. Wavelength, 3 mm. Line color is varied to help distinguish the individual trajectories.

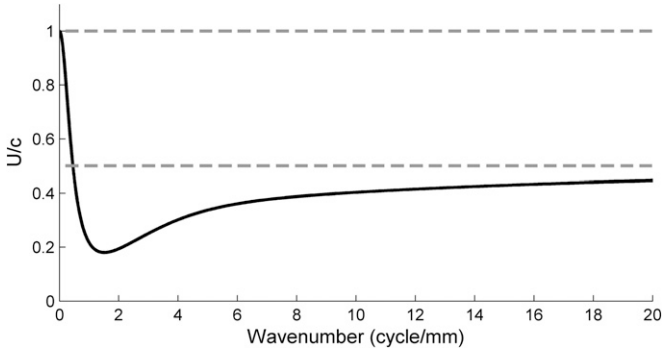

Fig. S2. Strongly dispersive character of fanning waves, illustrated by the ratio *U*/*c* of group velocity *U* and phase velocity *c*. Minimum value of *U*/*c* was 0.16. The two dashed lines mark the constant *U*/*c* ratios of shallow waves (*Upper*) and deep 2D waves (*Lower*).

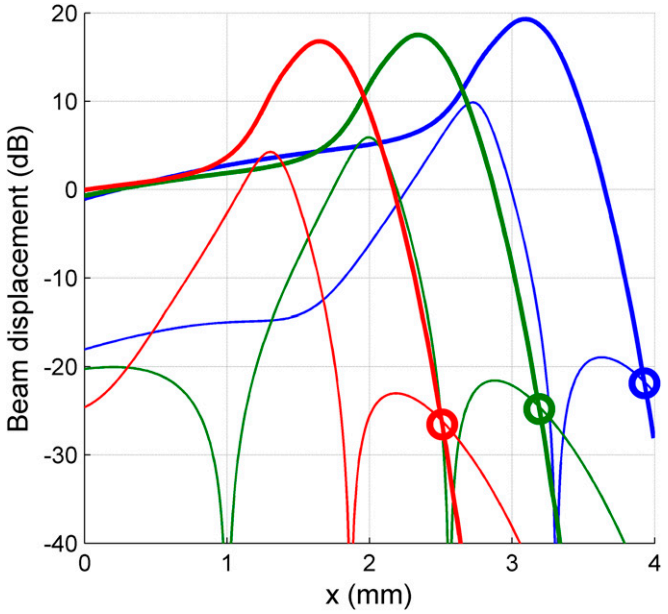

Fig. S3. Decomposition of beam displacement from Fig. 5*B* into contributions from AP mode (thick lines) and PA mode (thin lines). The initial growth of the PA mode originates from mode conversion. The subsequent notch corresponds to a change in sign of the contribution of the PA mode shape to the beam motion. Circles mark the points at which the PA mode finally becomes dominant over the AP mode.

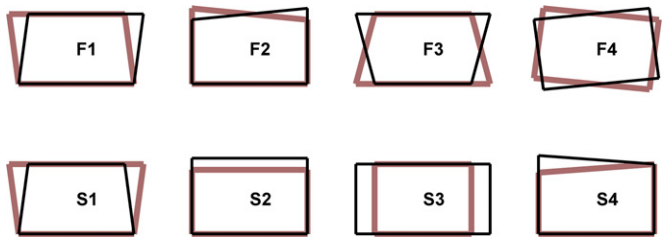

Fig. S4. Alternative geometries leading to fanning waves and squirting waves. Each pair of overlapping quadrangles represents the cross-section of the tunnel in which fluid is trapped. The two members of each pair depict the two extreme states of deformation and/or displacement during the cycle of the vibration. The upper row (F1–F4) shows vibration modes that preserve the tunnel cross-section and give rise to fanning waves if the tunnel is surrounded by fluid. Note that it is not necessary to have fluid chambers on both sides of the tunnel. The lower row (S1–S4) shows vibrations that change the cross-section and will give rise to squirting waves.